Journal of Electroceramics, 9, 87–100, 2002
© 2003 Kluwer Academic Publishers. Manufactured in The Netherlands.

A Mathematical-Physical Model for the Charge Transport in p-Type $SrTiO_3$ Ceramics Under dc Load: Maxwell-Wagner Relaxation

TH. HÖLBLING,[1] N. SÖYLEMEZOĞLU[2] & R. WASER[1,3]

[1] *Institut für Werkstoffe der Elektrotechnik, RWTH Aachen, D-52056 Aachen, Germany*

[2] *Byzanzsoft GmbH, D-60329 Frankfurt/Main, Germany*

[3] *Institut für Festkörperforschung, Research Center Jülich, D-52425 Jülich, Germany*

Submitted June 14, 2002; Revised September 3, 2002; Accepted October 18, 2002

Abstract. A mathematical-physical model to describe the current response of p-type $SrTiO_3$ ceramics in the low-temperature regime upon dc voltage step was developed, utilizing the numerical class library DIFFPACK™ (Numerical Objects, Norway). The current response in the time domain shows the experimentally observed Maxwell-Wagner relaxation (space charge polarization), followed by leakage current, and, eventually, resistance degradation. The relaxation behavior is analyzed by means of the simulation results for the spatial profiles of the electrical potential and the respective point defects. The impact of bias voltage and grain boundaries on the relaxation time is investigated. The simulation results are compared with experimental data.

Keywords: large-signal charge transport, grain boundaries, oxygen vacancy migration, numerical simulation model, Maxwell-Wagner relaxation, strontium titanate

1. Introduction

Through the past decades, the electronic properties of perovskite titanates were in the focus of extensive research, due to their versatile suitability for technical applications, e.g. varistor, capacitor dielectrics, PTC resistor [1]. Hereby, strontium titanate ($SrTiO_3$) was commonly employed as a model material for perovskites, due to its well-understood defect chemistry and conduction mechanisms [2]. In Fig. 1 (so-called *Kröger-Vink diagram* [3]) the typical dependence of the concentration of bulk defects in acceptor-doped (p-type) $SrTiO_3$ on equilibrium oxygen partial pressure p_{O_2} are displayed for both high equilibration temperatures (HT) and low temperatures <700 K (LT, thick lines). Insulating properties such as utilized for ceramic multi-layer capacitors (CMC) are obtained by an annealing step under moderately reducing atmospheres, and subsequent rapid cooling to low temperatures (so-called *quenching*). This leads to the following relation between the concentration of charged acceptor $[A']$ (here assumed as monovalent), the twofold ionized oxygen vacancies $[V_O^{\bullet\bullet}]$, electrons n, and holes p:

$$[A'] \approx 2[V_O^{\bullet\bullet}] \gg p \gg n \tag{1}$$

Due to the predominant impact of the ionic defects on space charge, a Brouwer condition for bulk electroneutrality applies [4]: $[A'] \approx 2[V_O^{\bullet\bullet}]$.

At low temperatures, the oxygen vacancies $V_O^{\bullet\bullet}$ are the only mobile ionic species. Their mobility $\mu_{V_O^{\bullet\bullet}}$ is strongly dependent on temperature T. With the $V_O^{\bullet\bullet}$ activation energy from Reference [5] and an anchor value of $\mu_{V_O^{\bullet\bullet}} = 10^{-8}\,\frac{\text{cm}^2}{\text{Vs}}$ at 500 K, one gets

$$\mu_{V_O^{\bullet\bullet}}(T) = \frac{2.316 \times 10^3}{T/\text{K}} \cdot \exp\left(-\frac{0.86\,\text{eV}}{kT}\right)\frac{\text{cm}^2}{\text{Vs}} \tag{2}$$

k is the Boltzmann constant.

Even though p is lower than $[V_O^{\bullet\bullet}]$ by many orders of magnitude, there may arise a significant contribution to electric conductivity from the holes, due to their high mobility μ_p (approx. $0.5\,\frac{\text{cm}^2}{\text{Vs}}$ at 500 K [6]) with respect to the $V_O^{\bullet\bullet}$. This leads to a mixed ionic/electronic conductor (MIEC) [7].

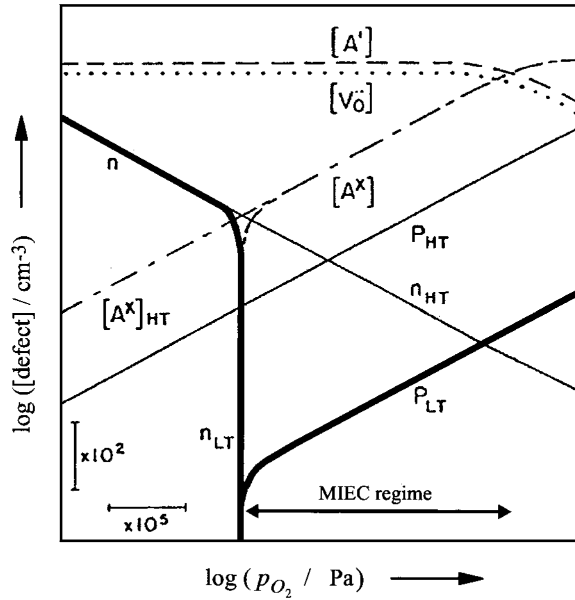

Fig. 1. Bulk point defect concentrations in p-type $SrTiO_3$ as a function of the oxygen partial pressure p_{O_2} during equilibration, for both high temperatures (HT) and low temperatures after quenching (LT, $T < 700$ K). At low temperatures and moderately large p_{O_2}, where the material acts as mixed ionic/electronic conductor (MIEC), the relation $n \ll p \ll [A'] \approx 2[V_O^{\bullet\bullet}]$ is valid (Graph taken from [8]).

In addition to the up to now well-understood bulk properties [8, 9], the electrical behavior of $SrTiO_3$ ceramics is greatly determined by the grain boundaries (GBs). This is elucidated by Fig. 2 where the current response of p-type $SrTiO_3$ (here as the geometry-independent absolute value of the complex electric conductivity $\underline{\sigma}$, i.e. the ratio of current response and electric field) upon a dc voltage step is displayed for a single crystal (subscript: sc) and both a coarse-grained (subscript: cg) and a fine-grained (subscript: fg) ceramic. It is apparent that the current response for all three characteristic regimes in the time domain, namely Maxwell-Wagner relaxation (initial decay of the current at short times) constant leakage current, and resistance degradation (i.e. the pronounced increase of the leakage current with the time) are unequivocally dependent on the grain size, or the number of GBs in the material, respectively.

A summary of grain boundary (GB) properties in p-type $SrTiO_3$ and existing models to describe the defect chemical and electrical scenario at GBs will be given in the upcoming section.

1.1. Grain Boundary Properties and Modeling

The existence of highly resistive GB layers in p-type $SrTiO_3$ have been postulated by impedance spectroscopy results in the 80es of the last century [11–15]. A Schottky model for GBs assuming additional defect states at the interface with respect to the grain interior, that create a space-charge layer depleted of mobile charge carriers, was brought about by Waser [16], and Chiang and Takagi [17]. The related intrinsic potential barrier at GBs denotes according to Schottky theory [18, 19]:

$$\varphi_{GB,0} = \frac{Q_{GB}^2}{8q_0\varepsilon[A']} \tag{3}$$

where Q_{GB} is the charge density of the GB donors. Q_{GB} can be converted into an equivalent space charge density ϱ_{GB} by taking into account the thickness of the crystallographic mismatch zone at the GB interface d_{interf}, according to:

$$\varrho_{GB} = \frac{Q_{GB}}{d_{interf}} \tag{4}$$

This is in general advantageous for GB modeling purposes, since it allows one to treat the GB states analogously to the zero-dimensional charged bulk defects. $[A']$ is the concentration of charged acceptors in the space charge depletion layer that is assumed constant in Eq. (3). q_0 is the elementary charge, ε the dielectric constant. ε at GBs is approx. the respective bulk value [20].

The extension of the space charge depletion layer d_{GB}, which exceeds d_{interf} by far, denotes:

$$d_{GB} = \frac{Q_{GB}}{q_0[A']} \tag{5}$$

For the electrical characterization of $SrTiO_3$ ceramics at a simplified descriptive level, the so-called *brick-wall model*, or at even less complexity, the *brick-layer model*, have commonly been employed [21]. Hereby, all grains are assumed to be of identical cubic shape with the characteristic edge length, i.e. grain size, d_{gr}, and all GBs are assumed to have identical properties, resulting in a homogeneous d_{GB}. Bulk and GB depletion layer are each assigned effective resistance and capacitance, R_B and C_B for the bulk, and R_{GB} and C_{GB} for the GBs. By those means, the ceramic can

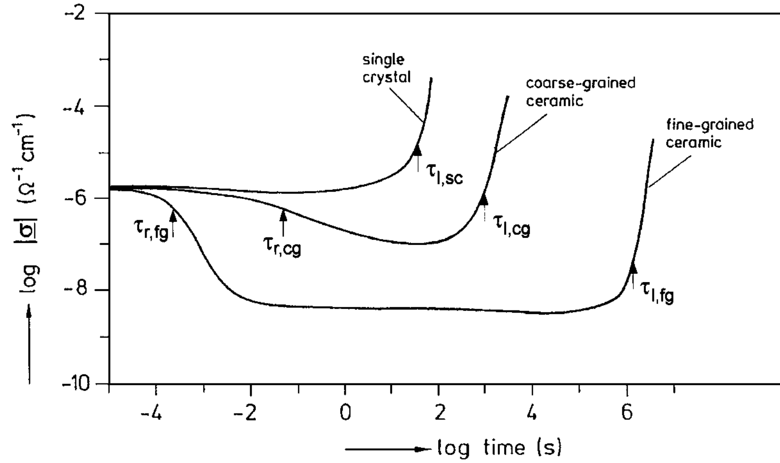

Fig. 2. Current response (here displayed as geometry—independent absolute value of complex conductivity σ) of p-type $SrTiO_3$ in the low-temperature regime ($T = 600$ K) after a dc voltage step of 31.25 V, for different microstructures. The dc bias is large enough to exceed the characteristic onset voltage for resistance degradation in all presented cases, thus leading to a pronounced long-term of leakage current in (a) single crystal (sc) (b) coarse-grained ceramic (cg), and (c) fine-grained ceramic (fg). Three characteristic regimes are discernible: (I) Short-term Maxwell-Wagner relaxation (characteristic relaxation time τ_r) (II) Stationary state leakage current (III) Long-term resistance degradation (characteristic lifetime τ_l where the current has reached a value that is one order of magnitude above its minimum) (Graph taken from [10]).

be modeled into an equivalent electrical circuit (see also Section 2). This has proven to be beneficial for separating GB and bulk related quantities from experimental data, like spectra of complex impedance [22] or voltage-step measurements in the time domain [23–25]. Yet, spatial variations of the electrical and defect chemical quantities, that obviously occur within the space charge depletion layer at GBs, are disregarded hereby. Generally, the employment of an equivalent electric circuit with constant elements according to the brick-wall model implies the assumption of a linear, time-invariant (LTI) system. This demands that the effective electric conductivity of the bulk, σ_B, and the GBs, σ_{GB}, remain constant, i.e. that the material shows ohmic behavior.

However, there is strong evidence that under sufficiently large bias, the defect chemical scenario at GBs as well as in the bulk, hence, the electrical behavior of ceramics, is changing significantly with time, leading to varistor effect and, eventually, resistance degradation [8]. Thus, for the latter phenomena, the assumption of constant R_B and R_{GB} cannot be maintained. Hence, their description exceeds the capability of the brick-wall model that restricts one to the small-signal (ohmic) regime.

Utilizing sophisticated numerical methods (finite element (FE) and finite difference (FD) calculations), refined models for the electrical properties of $SrTiO_3$ ceramics to overcome the above-stated limits were brought about:

Based on the Schottky depletion layer model, a mathematical-physical model for the defect chemical and electrical scenario at GBs in p-type $SrTiO_3$ in the electrostatic equilibrium state was developed, which allows the simulation of the spatial profile of the electrical potential and defect concentrations, thus the determination of $\varphi_{GB,0}$ and d_{GB} [26].

For the charge transport under bias, i.e. the non-equilibrium case, a number of theoretical approaches have come up over the past years: From the results of the above-mentioned electrostatics model, small-signal impedance spectroscopy simulation in the frequency domain were performed [27], which matched excellently with experimental results [28], thus confirming the validity of the GB Schottky depletion layer model. The influence of the geometric orientation of GBs on the impedance spectra of p-type $SrTiO_3$ in the small-signal regime was investigated [29, 30]: It was shown that even though distinct deviations of the grain shape from the ideal brick-wall microstructure may affect the impedance spectra both qualitatively (deviation from the two-arc shape) and quantitatively (depression of the GB semicircle), different effects may cancel in real ceramics and the brick-wall model can still represent a

good approximation in many cases. Utilizing Schottky diffusion theory [31], analytical expressions for the dc bias dependence of the leakage current in the course of voltage-step experiment, and for the voltage dependence of the GB potential barrier, i.e. varistor behavior, were developed [32]. By means of a mathematical-physical model for charge transport under large dc bias, resistance degradation in p-type $SrTiO_3$ was investigated [33]. Other than the electrostatics model, a spatial resolution of GB areas is not accomplished therein, and short-term current behavior is not regarded. A spatial resolution of the GB interface region was provided by a model for chemical diffusion simulations through GBs [34, 35], to study the concentration profile of point defects at the GBs. Since linear transport theory is applied, the model is restricted to the small-signal regime.

1.2. Motivation

In the present work, a mathematical-physical model for the simulation of the charge transport across GBs in p-type $SrTiO_3$ in the time domain for arbitrary voltages with a spatial resolution of the GB areas is proposed, which, to the best knowledge of the authors, has not been brought about yet. The model will focus on MIEC materials in the low-temperature regime, due to the relevance of said scenario for technical applications. The simulation results are to deliver the evolution of the spatial profiles of physical quantities such as the electrical potential and the defect concentrations, and the current response for all characteristic regimes in the time domain. This should lead to a better knowledge of the influence of the eletronic and defect chemical scenario at GBs on the charge transport. By means of the model, the phenomenon of Maxwell-Wagner relaxation (space charge polarization) will be discussed. Long-term conductivity (leakage current) and its dependence on the dc bias (varistor behavior) have been discussed in [36]. Resistance degradation will be in the focus of further contributions [37].

2. Mechanism of Maxwell-Wagner Relaxation

Maxwell-Wagner relaxation occurs in media that show inhomogeneous electrical conductivity, such as p-type $SrTiO_3$ ceramic. Voltage-step measurements, i.e. the recording of the current response upon a dc voltage step, reveals a characteristic decay of the electric current density $i(t)$ that yields an exponential law: $i(t) = i_0 \cdot \exp(-\frac{t}{\tau_r})$, with the relaxation time τ_r. This is due to the pile-up and the depletion of mobile charge carries that arise at the interface between highly conducting and lowly conducting phases, which leads to space charge polarization. The electric field E_{pol} that is caused by the polarization charges does counteract the external electric field E_{ext} from the dc bias voltage U_{DC}, thus leading to a net material field E that is lower than E_{ext}. In term, this reads that U_{DC} will mainly drop across the lowly conducting material regions. If the resistance of the lowly conducting phase is finite, $i(t)$ will not drop to zero, but a constant leakage current will settle after Maxwell-Wagner relaxation.

In Fig. 3, the Maxwell-Wagner relaxation current for p-type $SrTiO_3$ after a voltage step is displayed, here again as the absolute value of $\underline{\sigma}$, i.e. the ratio of $i(t)$ and E_{ext} (with $E_{ext} = \frac{U_{DC}}{d}$, where d denotes the thickness of the ceramic).

Taking into account the brick-wall model (see Fig. 3(b)), neglecting the impact of electrodes [8] and highly-conducting current paths perpendicular to the electrodes, i.e. $R_l \to \infty$ [28], and assuming the obvious relations $R_{GB} \gg R_B$ and $C_{GB} \gg C_B$, the current plateau for short times is ascribed to the bulk, whereas that for long times, i.e. the stationary state after Maxwell-Wagner relaxation, is ascribed to the sum of bulk and GB resistance. The current decay is due to the charging of the GB capacitance that is characterized by τ_r:

$$\tau_r = R_B \cdot C_{GB} \tag{6}$$

The effective electrical conductivity of bulk σ_B and GB depletion layer σ_{GB} can be extracted from the voltage-step experiment solely by geometry parameters, namely d and d_{gr} [5, 28].

In this contribution the mechanism of Maxwell-Wagner relaxation will be closely investigated by means of simulation results that are obtained from the mathematical-physical model for charge transport in p-type $SrTiO_3$ ceramics. The model will be outlined in the upcoming section.

3. Simulation Model

The geometry of the simulation model consists of a one-dimensional longitudinal cross-section through a

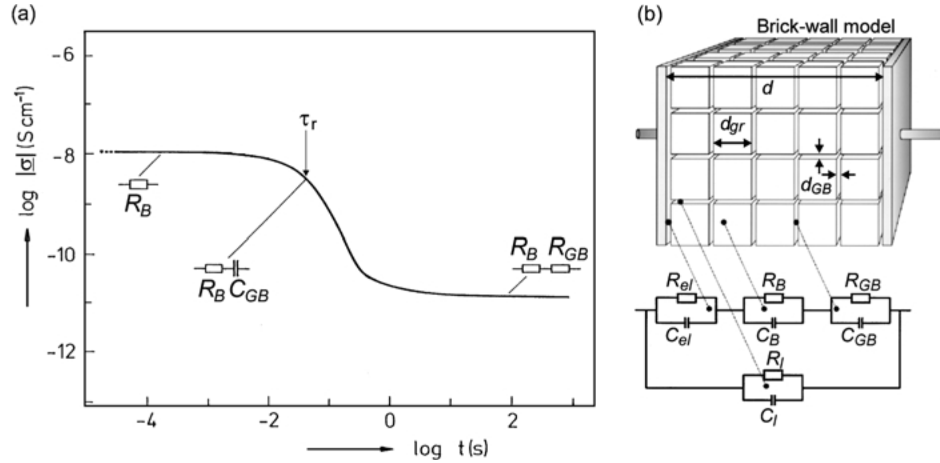

Fig. 3. (a) Typical current response (here displayed as geometry-independent absolute value of complex conductivity $\underline{\sigma}$) of a p-type (Ni-doped) $SrTiO_3$ ceramic, after a dc voltage step of 10 V, measured at 483 K. The dopant concentration is 1.6×10^{19} cm^{-3}. The sample thickness is 1 mm, the average grain size d_{gr} is 2 μm (b) Schematic of the brick-wall model for polycrystalline material (thickness d, average grain size d_{gr}, GB depletion layer width d_{GB}), and equivalent electrical circuit: each material phase (electrodes, bulk, GB depletion layers) are modeled into a parallel circuit, consisting of resistance R and capacitance C (subscripts: el = electode, B = bulk, GB = grain boundary, l = current paths along GBs). In the low-temperature regime, electronic inversion phenomena at GBs that may cause highly conducting current paths along GBs do not occur, thus allowing R_l and C_l to be neglected (Graphs taken from [10]).

p-type $SrTiO_3$ ceramic, its extensions into the other two space dimensions are assumed to be infinite. This simplification is encouraged by Hagenbeck who utilized results from simulation of one single GB to shape the impedance spectra of an extended ceramic that contains a large number of GBs (see Section 1.1), and achieved an excellent match between simulation and experiment [28].

The material is regarded as a continuous medium according to Maxwell's theory. Hence, the periodical atomic lattice structure may be neglected and the employment of macroscopic physical quantities such as relative dielectric permittivity ε_r is allowed.

The model is based on the approach of point defect chemistry: apart from the overall impact of the electrodes and GBs, a statistical distribution of zero-dimensional electronic and ionic defects is assumed to greatly determine the material properties of the bulk, i.e. volume effects outweigh those effects which may arise from the presence of so-called *extended defects* in the grain interior. (It should be noted nevertheless that evidence has been found which, besides point defects, supports the impact of extended defects on the behavior of $SrTiO_3$ single crystals [38–40]).

The model utilizes Schottky diffusion theory [18, 19, 31], i.e. particle transport in bulk and interface regions can be described by Nernst-Planck transport equations for the particle current density of electrons j_n, holes j_p, and oxygen vacancies $j_{V_O^{\bullet\bullet}}$:

$$j_n = -D_n \cdot \frac{\partial n}{\partial x} - \mu_n \cdot n \cdot E \tag{7}$$

$$j_p = -D_p \cdot \frac{\partial p}{\partial x} + \mu_p \cdot p \cdot E \tag{8}$$

$$j_{V_O^{\bullet\bullet}} = -D_{V_O^{\bullet\bullet}} \cdot \frac{\partial [V_O^{\bullet\bullet}]}{\partial x} + \mu_{V_O^{\bullet\bullet}} \cdot [V_O^{\bullet\bullet}] \cdot E \tag{9}$$

D_n, D_p, and $D_{V_O^{\bullet\bullet}}$ are the diffusion coefficient of electrons, holes, and $V_O^{\bullet\bullet}$, respectively, and μ_n is the mobility of electrons. Mobility and diffusion coefficient of the species i are coupled via Nernst-Einstein relation: $\mu_i = \frac{z_i q_0}{kT} \cdot D_i$, where z_i denotes the charge number of the species ($z_n = -1$ for electrons, $z_p = 1$ for holes, and $z_{V_O^{\bullet\bullet}} = 2$ for $V_O^{\bullet\bullet}$). The formulation of Eqs. (7)–(9) does allow local gradients of D_i or μ_i, respectively, that might occur e.g. due to reduced mobility of the $V_O^{\bullet\bullet}$ at GBs, as it is assumed in Reference [34].

The local change of the concentration of the mobile charge carriers is described by continuity equations.

Due to the very short mean free path of the electronic charge carriers with respect to e.g. classical semiconductors [33], local electronic equilibrium will always be assumed, i.e., from the local concentration of holes

$p(x)$, the local concentration of electrons $n(x)$ can be unequivocally calculated, and vice versa:

$$n(x) = \frac{n_i^2}{p(x)} \Leftrightarrow p(x) = \frac{n_i^2}{n(x)} \tag{10}$$

where n_i is the intrinsic electronic charge carrier concentration. This allows one to restrict the model to only one continuity equation for the electronic charge carriers. Usually, an equation for the majority carriers, namely the holes, is utilized. One gets for $V_O^{\bullet\bullet}$ and p:

$$\frac{\partial [V_O^{\bullet\bullet}]}{\partial t} = \frac{\partial}{\partial x}\left(D_{V_O^{\bullet\bullet}} \cdot \frac{\partial [V_O^{\bullet\bullet}]}{\partial x}\right) - \frac{\partial}{\partial x}(\mu_{V_O^{\bullet\bullet}} \cdot [V_O^{\bullet\bullet}](x) \cdot E(x)) + q_{V_O^{\bullet\bullet}}(x) \tag{11}$$

$$\frac{\partial p(x)}{\partial t} = \frac{\partial}{\partial x}\left(D_p \cdot \frac{\partial p(x)}{\partial x}\right) - \frac{\partial}{\partial x}(\mu_p \cdot p(x) \cdot E(x)) + q_p(x) \tag{12}$$

$q_{V_O^{\bullet\bullet}(x)}$ and $q_p(x)$ denote additional source terms of $V_O^{\bullet\bullet}$ and holes that describe the amount of concentration change which is not caused by particle transport but by e.g. internal defect chemical reactions.

For the interaction between the electrical potential φ and the charged defects Poisson's equation is employed.

$$\Delta\varphi = -\frac{\varrho}{\varepsilon} \tag{13}$$

ϱ denotes the local space charge density that is composed of the sum of the concentration of all mobile and immobile charged species c_i, weighted by z_i.

$$\varrho(x) = q_0 \cdot \sum_i z_i \cdot c_i(x) \tag{14}$$

The ohmic current density i_{ohmic} is obtained by summing up the particle current densities according to Eqs. (7)–(9), weighted by the individual charge of the respective species:

$$i_{ohmic} = q_0 \cdot (z_n j_n + z_p j_p + z_{V_O^{\bullet\bullet}} j_{V_O^{\bullet\bullet}}) \tag{15}$$

Eventually, the total electric current density i is obtained by $i = i_{ohmic} + i_{disp}$, with i_{disp} being the dielectric displacement current:

$$i_{disp} = \frac{1}{\varepsilon}\frac{\partial E}{\partial t} = -\frac{1}{\varepsilon}\frac{\partial}{\partial t}\frac{\partial \varphi}{\partial x} \tag{16}$$

The scenario at the borders of the model geometry is determined by the choice of boundary conditions (BCs) for the system state quantities n, p, $[V_O^{\bullet\bullet}]$, electrical potential, and partial current density $j_{V_O^{\bullet\bullet}}$ and j_p (see Fig. 4). The subscript *anodic* refers to the site of higher electrical potential, the subscript *cathodic* to the site of lower electrical potential. Two different boundary scenarios are considered, namely systems that are bounded by electrodes ("closed" boundaries, see Fig. 4(a)), and boundaries that are situated in undisturbed bulk regions off the GB interfaces ("open" boundaries, see

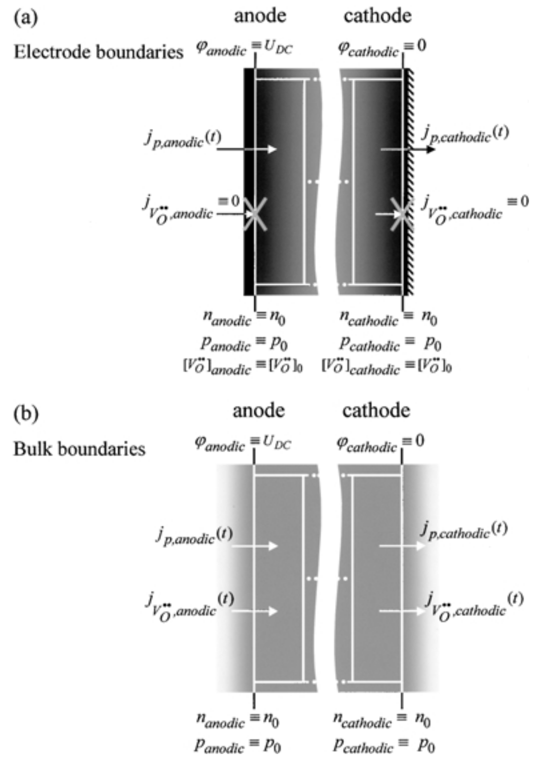

Fig. 4. Illustration of the scenario at the borders of the model geometry for the charge transport in $SrTiO_3$ where boundary conditions (BCs) apply for various physical quantities, i.e. electrical potential φ, particle concentrations $[V_O^{\bullet\bullet}]$, n, and p, and particle currents $j_{V_O^{\bullet\bullet}}$ and j_p (the subscript 'anodic' relating to the site at higher electrical potential, 'cathodic' to the site at lower electrical potential). Different BCs emerge for (a) electrode boundaries, here assumed as completely blocking for oxygen transfer (b) system boundaries situated in the bulk.

Fig. 4(b)). Whereas the further are to describe the usual case of material embedded between two electrodes, the latter will be employed to somewhat "extract" the impact of GBs only.

Considering non-catalytic electrode material (e.g. gold) [41], oxygen exchange at the system boundaries may be neglected, due to the sluggish surface reaction kinetics in the low-temperature regime that is regarded here [42, 43]. This leads to vanshing $j_{V_O^{\bullet\bullet}}$ at the electrodes, thus constant overall amount of $V_O^{\bullet\bullet}$ within the material. This is described by *Neumann* BCs for $j_{V_O^{\bullet\bullet}}$.

The electrodes are modeled as flat-band electrodes, i.e. an initial band-bending at the electrodes in the electrostatic equilibrium case is neglected. The electrochemical potential of the electronic charge carriers at the electrode is assumed to be constant over time, thus leading to constant particle concentrations n_0 and p_0 at the boundaries, i.e. *Dirichlet* BCs. n_0 and p_0 are equal to the bulk concentration of the electrons and holes at electrostatic equilibrium.

Dirichlet BCs for the electronic charge carriers will as well apply for "open", or bulk boundaries, far off the GB interfaces. Furthermore, since in contrast to electrode boundaries $j_{V_O^{\bullet\bullet}}$ will not be hampered by bulk boundaries, Dirichlet BCs, i.e. constant equilibrium concentration $[V_O^{\bullet\bullet}]_0$, rather than Neumann BCs, will be chosen in the case of bulk boundaries.

Another set of Dirichlet BCs is employed for the electrical potential: the difference between the fixed potential values at the anode and at the cathode denotes the dc bias voltage U_{DC}.

Energy levels following the band diagram are assigned to the point defects for describing the defect chemical reactions in the material (acceptor ionization, GB charge trapping) according to Fermi-Dirac statistics [44–46]. All point defects are modeled as spatial profiles of particle volume concentrations.

The GB donor states are assumed as additional point defects whose occurrence be restricted to the GB mismatch zone. Browning's suggestion of "shallow" donors with an energy level slightly below the conduction band similar to the bulk $V_O^{\bullet\bullet}$ is embodied [47].

Inversion layers at GBs [28] that might lead to short-circuit current paths between the electrodes (see Fig. 3) are neglected.

The start-up values for the simulation under applied bias, that comprise the bulk equilibrium concentrations which are employed as Dirichlet BCs, are obtained by an initial electrostatics simulation according to the simulation algorithm of Hagenbeck [26].

A spatial resolution is obtained by laying an adaptive finite element mesh upon the model geometry.

The model equations are solved by employing routines from the numerical class library DIFFPACK™ (Numerical Objects, Norway) [48, 49].

4. Simulation Results

In the following, simulation results are discussed for the case that a voltage-step is applied to a bicrystal model geometry of p-type $SrTiO_3$ in the quenched mode after cooling from moderately reducing atmosphere.

For all simulations, the following input parameters apply: The length of the model geometry is $d = 1\ \mu$m. For the GB interface, an extension $d_{interf} = 1$ nm is assumed [23]. GB diffusion coefficient and mobility are of the respective bulk values. The GB donor state density is 8×10^{20} cm^{-3}, which is equivalent to a GB charge density of $Q_{GB} = 1.28 \times 10^{-5}\ \frac{\text{C}}{\text{cm}^2}$. The acceptor concentration $[A']$ amounts 2×10^{19} cm^{-3}. For the sake of simplicity, the acceptor is regarded as "shallow", with an energy level close to the valence band that leads to completely ionized acceptor states. The relative dielectric permittivity ε_r is 150, at a temperature $T = 500$ K. According to Eq. (3), utilizing Eq. (4), this leads to an equilibrium GB potential barrier heigth $\varphi_{GB,0} \approx 0.5$ eV.

First, for electrode ("closed") boundaries, a general simulation is performed, which provides an overview of all characteristic regimes of the current response in the time domain. Moreover, by means of the evolution of the related spatial profiles of distinct physical quantities until the steady state, the mechanism of Maxwell-Wagner relaxation is investigated. Second, by simulation sequences with bulk ("open") boundaries which are employed to exclude the influence of the electrodes, the sole impact of the external bias and the grain size on Maxwell-Wagner relaxation are investigated in detail. Eventually, simulation results are compared with experimental data.

4.1. Current Response

In Fig. 5 the simulated current response $i(t)$ upon a dc bias voltage step of $U_{DC} = 0.47$ V at $t = 0$ with electrode ("closed") boundaries is displayed. Three distinguished regimes are discernible:

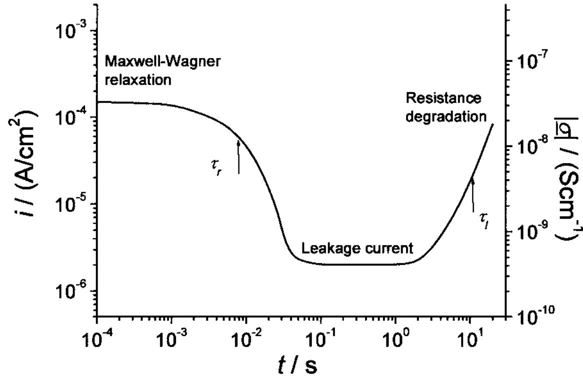

Fig. 5. Simulated current response and absolute value of complex conductivity $\underline{\sigma}$ of a p-type $SrTiO_3$ bicrystal model structure (acceptor concentration: 2×10^{19} cm^{-3}, GB donor charge density: $Q_{GB} = 1.28 \times 10^{-5} \frac{C}{cm^2}$) in the low-temperature regime ($T = 500$ K) after a dc voltage step of $U_{DC} = 0.47$ V, exceeding the onset voltage for resistance degradation, thus leading to a pronounced increase of leakage current after Maxwell-Wagner relaxation and stationary state.

1. Maxwell-Wagner relaxation, i.e. the decay of $i(t)$ from a bulk-determined start-up value with the relaxation time τ_r.
2. A constant leakage current that is determined by the electronic conductivity in the GB depletion layer [36].
3. Resistance degradation, i.e. the strong increase of $i(t)$ at advanced time with the characteristic lifetime τ_l [37].

This qualitatively correlates well with the experimental results for p-type $SrTiO_3$ ceramics displayed in Fig. 2.

As stated earlier, it is the phenomenon of Maxwell-Wagner relaxation that will be in the focus of this contribution: Based on the simulation results for the temporal evolution of the spatial profile of the defect concentrations, electrical potential, and space charge density, that each refer to the Maxwell-Wagner regime in Fig. 5, the underlying relaxation mechanism will be investigated.

4.2. Evolution of the Spatial Profile of the Oxygen Vacancies

Simulation results for the overall shift of $[V_O^{\bullet\bullet}]$ with time upon a dc voltage step are presented in Fig. 6(a), whereas a detailled "zoom" into the GB area is provided by Fig. 6(b). The latter reveals a noticeable shift of the $V_O^{\bullet\bullet}$ into and from the space charge depletion layer that unequivocally form at the GBs. This local accumulation/depletion effect supports the general assumption of a blocking character of the GBs for $V_O^{\bullet\bullet}$ [33, 34].

The shift of the $V_O^{\bullet\bullet}$ at the GBs under dc bias represents the mechanism of space charge polarization, i.e. Maxwell-Wagner relaxation: According to Eq. (1), the $V_O^{\bullet\bullet}$ are the only mobile charge carriers that significantly influence the space charge. The charge shift between the electrodes and adjacent GBs (or between neighboring GBs when a polycrystal is considered) that is accompanied by $V_O^{\bullet\bullet}$ migration causes a de-electrifying polarization field that weakens the external electric field which is built up by U_{DC}. As a consequence, the gradient of the electrical potential in the bulk areas is diminishing in the course of $V_O^{\bullet\bullet}$ redistribution (see also Fig. 6(c)). This leads to the decay of $i(t)$. Furthermore, due to the blocking character of the electrodes for ionic transport, $V_O^{\bullet\bullet}$ are neither allowed to enter nor to leave the material. As a result, one obtains classical Debye-Hückel polarization [50]: an accumulation of $V_O^{\bullet\bullet}$ at the cathode is accompanied by a depletion of the $V_O^{\bullet\bullet}$ at the anode (see Fig. 6(a)).

It is worth mentioning that whereas the $V_O^{\bullet\bullet}$ profile at the GB has reached its steady state after relatively short times (i.e. at the end of Maxwell-Wagner relaxation), the overall redistribution of the $V_O^{\bullet\bullet}$ between the system boundaries, i.e. the electrodes, has not been completed at this juncture, but goes on in the course of resistance degradation. The depletion of the $V_O^{\bullet\bullet}$ at the cathode generally gives way for an additional space charge layer that is formed by the left-behind negative acceptor charges. In term, a pronounced positive space charge layer is formed at the anode by the accumulation of surplus $V_O^{\bullet\bullet}$.

Altogether, it is evident that a significant amount of charge can be stored both at the electrodes and at the GBs. This is hinted at by the capacitances C_{el} and C_{GB} in Fig. 6(a).

4.3. Evolution of the Spatial Profile of the Electrical Potential

Simulation results of the time dependence of the potential drop over the model geometry for p-type $SrTiO_3$ are presented in Fig. 6(c): Immediately after applying the dc voltage step, the voltage drops linearly from the

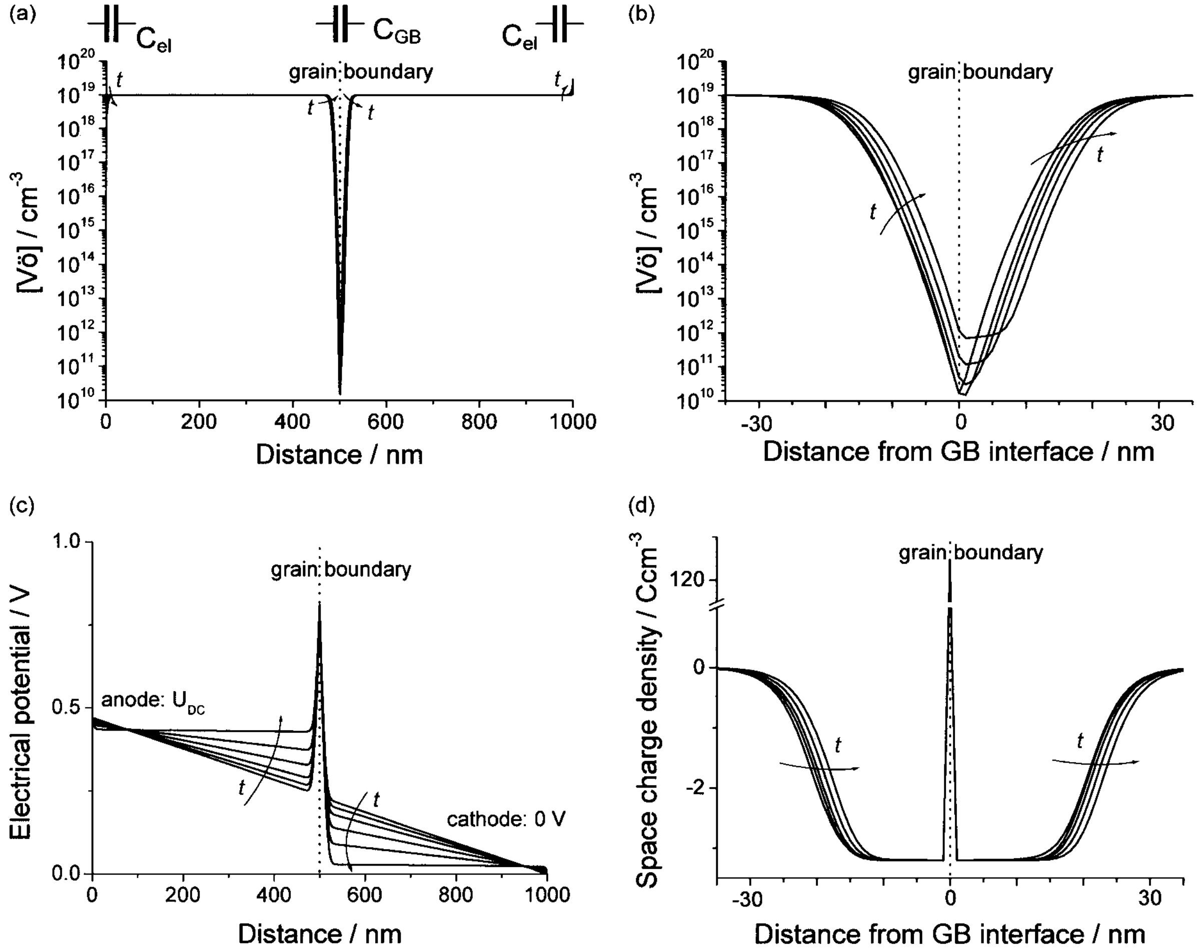

Fig. 6. Simulated evolution of the spatial profiles of (a) global oxygen vacancy concentration (b) GB oxygen vacancy concentration (c) electrical potential and (d) space charge density for a p-type $SrTiO_3$ bicrystal model structure in the low-temperature regime after a dc voltage step of 0.47 V, from $t = 0$ to 30 ms ($T = 500$ K, acceptor concentration: 2×10^{19} cm^{-3}, GB donor charge density: $Q_{GB} = 1.28 \times 10^{-5} \frac{\mathrm{C}}{\mathrm{cm}^2}$).

anode to the cathode over the bulk areas of the model geometry. At the GB, the resulting electrical potential is emerging from the superposition of the impact of the external bias and the intrinsic potential barrier over the Schottky depletion layer (see Eq. (3)).

In the course of Maxwell-Wagner relaxation the potential slope over the charge-free bulk regions is decaying with the shift of the $V_O^{\bullet\bullet}$ at the GBs, i.e. space charge polarization, due to the de-electrifying impact of the thus built-up polarization field (see also Fig. 6(d)).

After the leveling of the potential gradient in the bulk, i.e. after the diminishing of the electric field in the bulk, U_{DC} mainly drops at the GB and, to a smaller amount, at the electrodes. By then, redistribution of the $V_O^{\bullet\bullet}$ at the GB interface, i.e. space charge polarization, has been completed and a stationary leakage current has settled.

4.4. *Evolution of the Spatial Profile of the Space Charge Density*

Simulation results for the evolution of the space charge at the GB are displayed in Fig. 6(d): One clearly observes the large positive GB charge that is the cause of the negative GB space charge depletion layer.

The $V_O^{\bullet\bullet}$ redistribution at the GB interface under dc bias causes a shift of the depletion layer from the

anode to the cathode while—for not too large dc bias—its extension d_{GB} remains virtually unchanged with respect to the electrostatic scenario [36]. Taking into account Eq. (6) for the relaxation time τ_r and considering the dependence of the GB capacitance C_{GB} on d_{GB} : $C_{GB} \propto \frac{1}{d_{GB}}$, it is apparent that τ_r will be as well independent of U_{DC} (see Section 4.6).

4.5. Comparison with "Open" Boundary Model

In contrast to real ceramics where a large number of GBs outweigh the impact of electrodes on material behavior, the influence of electrodes may not be neglected for a bicrystal. Herein, the relaxation time will be affected by the electrode contribution to the overall capacitance. In order to "extract" the sole impact of GBs, "open" boundaries will be employed (see Fig. 4(b)). This will be legitimated for short simulation times, yet not for the long-term behavior: In the case of electrode boundaries $j_{V_O^{\bullet\bullet}}$ will unequivocally drop to zero in the course of the overall $V_O^{\bullet\bullet}$ redistribution. However, in the case of bulk boundaries, due to their non-blocking character for ionic transport, this will never be accomplished. Hence, by the choice of bulk boundaries, leakage current as well as resistance degradation cannot be described accurately.

The simulation results of the current response for both electrode and bulk boundaries with otherwise unchanged input parameters are displayed in Fig. 7.

Whereas the initial current remains unchanged for "open" boundaries due to virtually unchanged bulk conductivity, τ_r increases with respect to "closed" boundaries. This is due to the increase of the effective capacitance of the model geometry $C_{GB,eff}$ that arises from the "removal" of the electrode capacitances C_{el} from the equivalent serial electric circuit (see Fig. 6(a)) where only C_{GB} remains.

4.6. Variation of dc Bias Voltage and Number of GBs (Grain Size)

Based on a simulation model with bulk boundaries, the impact of the value of the dc voltage step U_{DC} and of different grain sizes d_{gr} on the current response during Maxwell-Wagner relaxation are investigated: For the variation of d_{gr}, an altering number of GBs n_{GB} with identical properties will be embedded into the model geometry, thus reducing d_{gr} with increased n_{GB}.

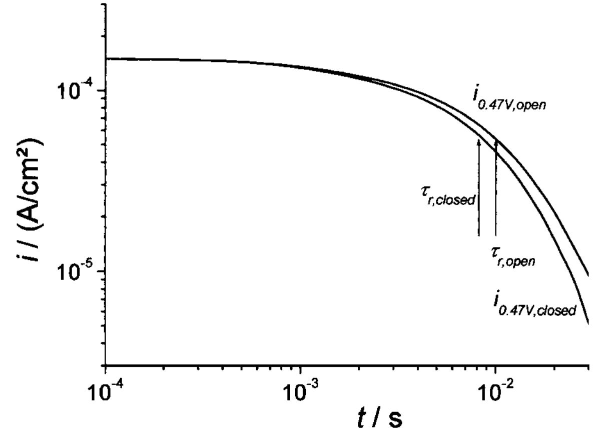

Fig. 7. Comparison of the simulation results of the current response for a p-type $SrTiO_3$ bicrystal model structure in the low-temperature regime after a dc voltage step of 0.47 V for electrode boundaries (relaxation time $\tau_{r,closed}$) and "open" boundaries (relaxation time $\tau_{r,open}$) (T = 500 K, acceptor concentration: 2×10^{19} cm^{-3}, GB donor charge density: $Q_{GB} = 1.28 \times 10^{-5}\ \frac{\text{C}}{\text{cm}^2}$).

The simulation results for $i(t)$ are displayed in Fig. 8.

As it was expected, τ_r does not vary with different values of U_{DC} (see Fig. 8(a)). Moreover, the initial current increases with increasing U_{DC}, revealing ohmic behavior for the regarded voltages.

In term, Fig. 8(b) shows the decrease of τ_r with increasing n_{GB}, i.e. decreasing d_{gr}. Again regarding a serial electric circuit, the effective capacitance with respect to n_{GB} denotes:

$$C_{GB,eff}(n_{GB}) = \frac{C_{GB}}{n_{GB}} \tag{17}$$

with $C_{GB,eff}(2) = \frac{C_{GB}}{2}$ and $C_{GB,eff}(3) = \frac{C_{GB}}{3}$. Since the total bulk resistance is only moderately increased by embedding two further GBs into the model geometry, we get for the ratio of τ_r from one to three GBs: $\tau_{r,1GB} \approx 2 \cdot \tau_{2GB} \approx 3 \cdot \tau_{3GB}$, which is in good accordance with Eq. (6).

Eventually, it is worth noting that the charge-trapping at GBs turned out to be negligible for the cases presented here. Nor is the ionization of acceptors any prerequisite for the discussed phenomena.

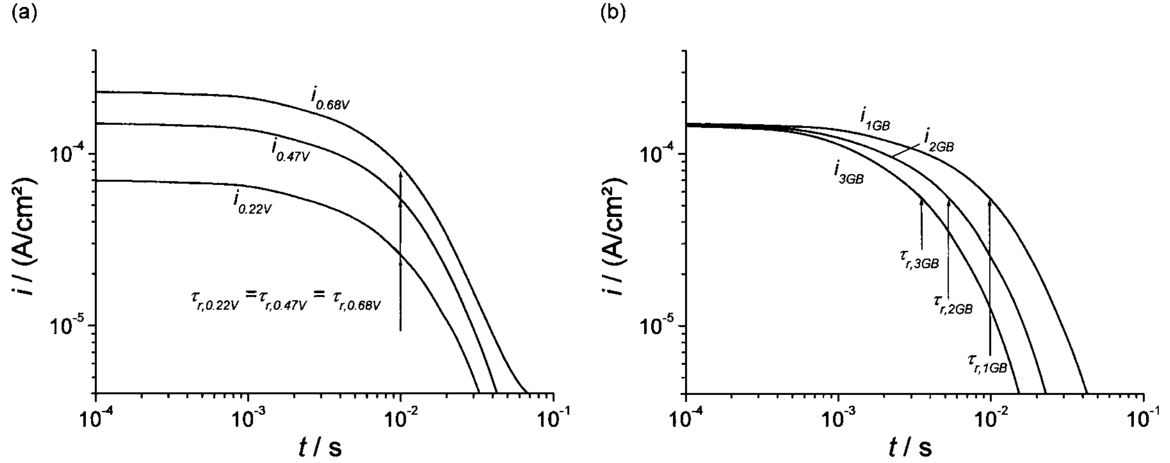

Fig. 8. Comparison of the simulation results of the current response for a p-type $SrTiO_3$ model structure in the low-temperature regime after a dc voltage step U_{DC} at (a) constant number of GBs ($n_{GB} = 1$) and different biases (0.22 V, 0.47 V, 0.68 V) (b) constant bias ($U_{DC} = 0.47$ V) and different n_{GB} (1 to 3) (i.e. different grain size). Simulation parameters: $T = 500$ K, acceptor concentration: 2×10^{19} cm^{-3}, GB donor charge density: $Q_{GB} = 1.28 \times 10^{-5}\ \frac{\text{C}}{\text{cm}^2}$.

4.7. *Extrapolation Towards Larger Geometries—Comparison with Experiment*

The simulation results for the bicrystal model geometry with bulk boundaries yield a relaxation time $\tau_{r,1} = 10^{-2}$ s (see Fig. 8(a)). For comparison with a real ceramic, the obtained results will be "fitted" to the voltage-step experiment displayed in Fig. 3(a):

In a first step, the model geometry is extrapolated to the thickness d_2 and the average grain size $d_{gr,2}$, or the number of GBs $n_{GB,2}$, of the real ceramic, and the simulated bulk conductivity $\sigma_{B,1}$ is adjusted to the temperature of the experiment T_2. Hereby, $\tau_{r,2}$ is obtained. This procedure is described in the Appendix. In a second step, the possibly different processing conditions of the real ceramic (here: Ni-doped $SrTiO_3$; sintering conditions: 1613 K, O_2, 6 h; annealing conditions: 973 K, $p_{O_2} = 10^5$ Pa, 8 h; Ni concentration: 1.6×10^{19} cm^{-3}) with respect to the assumptions for the simulation model, that might lead to different defect chemical scenario in the bulk, and hence to different σ for the real ceramic and the model geometry at T_2, will be considered. The thus obtained relaxation time $\tau^*_{r,2}$ is compared with the experimentally obtained relaxation time $\tau_{r,exp} = 0.04$ s of Fig. 3(a).

From e.g. the simulation results for $U_{DC} = 0.47$ V in Fig. 8(a), with the related short-term current density $i = 1.5 \times 10^{-4}\ \frac{\text{A}}{\text{cm}^2}$ and the extension of the model geometry $d_1 = 1\mu$m, one obtains from Eq. (A4): $\sigma_{B,1} = 3.19 \times 10^{-8}\ \frac{\text{S}}{\text{cm}}$. With the bulk value $[V_O^{\bullet\bullet}] = 1 \times 10^{19}$ cm^{-3} (see Fig. 6(a)) and $\mu_{V_O^{\bullet\bullet}}$ at $T_1 = 500$ K, a vanishingly small hole contribution to $\sigma_{B,1}$ arises from Eq. (A5). This allows one at first approximation to neglect holes for determinining $\sigma_{B,2}$ at $T_2 = 483$ K.

From Eqs. (2) and (A5), we obtain $\sigma_{B,2} = 1.64 \times 10^{-8}\ \frac{\text{S}}{\text{cm}}$.

With $d_2 = 1$ mm, $d_{gr,2} = 2\,\mu$m, and the simple formula $n_{GB} = \frac{d}{d_{gr}}$, we get $n_{GB,2} = 500$, whereas the GB number of our bicrystal model geometry $n_{GB,1}$ is, of course, one.

Inserting the above-accumulated data into Eq. (A3), we eventually obtain $\tau_{r,2} = 0.04$ s.

From Fig. 3(a), bulk conductivity of the ceramic sample immediately reads $\sigma_{B,exp} = 10^{-8}\ \frac{\text{S}}{\text{cm}}$.

Since $\sigma_{B,2}$ turns out larger than $\sigma_{B,exp}$ by a factor of approx. 1.64, we must multiply $\tau_{r,2}$ by this factor, to regard aforesaid possibly different processing conditions. The hereby obtained value $\tau^*_{r,2} = 0.066$ s matches well with the value $\tau_{r,exp}$ from the experiment. With respect to the simplicity of the employed model geometry, this hints at a rather homogeneous distribution of GB properties in p-type $SrTiO_3$ that has been observed by Rodewald by microelectrode impedance measurements on single GBs [24, 51].

5. Conclusions

1. A mathematical-physical model for charge transport processes in p-type $SrTiO_3$ polycrystals under dc load has been developed. The model describes all characteristic phenomena of the system evolution in the time domain, i.e. Maxwell-Wagner relaxation, stationary leakage current, and resistance degradation. It provides a spatial resolution of all relevant physical quantities such as defect concentrations and electrical potential, which allows investigation of the GB scenario in detail. The model is not limited to the small-signal regime but remains valid for arbitrarily large bias voltages.
2. By means of the simulation model, the phenomenon of Maxwell-Wagner relaxation was examined. The cause of space charge polarization is the $V_O^{\bullet\bullet}$ redistribution at the GBs under dc load. Both the impact of the overall GB capacitance (i.e. the number of GBs in the ceramics or the grain size, respectively) on Maxwell-Wagner relaxation time τ_r, and the independence of τ_r of the dc bias (for not too large biases) were confirmed. Extrapolation of the results for the model geometry and comparison with real extended ceramics show a good agreement between simulation and experiment.
3. The extension of the proposed simulation model towards 2-dimensional and eventually 3-dimensional geometries will gave way for a detailed investigation of the field and current distribution, and the related material stress within p-type $SrTiO_3$ polycrystals. This may also represent a vital step towards spatially resolved transient simulation of complete ceramic devices, which would generally support ceramic engineering.

Appendix: Extrapolation of Simulation Results to Extended Structures and Different Temperatures

Some formulae for fitting the simulation results for the bicrystal model geometry of p-type $SrTiO_3$ to extended structures and different temperatures are derived in this section.

Equation (6) for τ_r may be rewritten, regarding the brick-wall model (see Fig. 3(b)):

$$\tau_r = R_B \cdot C_{GB} = \frac{d_{B,tot}}{\sigma_B \cdot A_{B,tot}} \cdot \frac{\varepsilon \cdot A_{GB,tot}}{d_{GB,tot}} \tag{A1}$$

$A_{B,tot}$ and $A_{GB,tot}$ denote the effective area of the volume portion of the bulk and the GBs parallel to the electrodes, whereas $d_{B,tot}$ and $d_{GB,tot}$ denote the effective length of either material phase between the electrodes, respectively. The following obvious approximations are commonly employed:

- $A_{B,tot}$ and $A_{GB,tot}$ are approximately of the electrode area A.
- $d_{B,tot}$ is approximately of the total probe thickness d.
- $d_{GB,tot}$ equals $n_{GB} \cdot d_{GB}$, i.e. the number of GBs along a path from anode to cathode perpendicular to the electrodes, multiplied with the length of the Schottky depletion layer at one GB.

Then, Eq. (A1) simplifies to:

$$\tau_r \approx \frac{d}{\sigma_B} \cdot \frac{\varepsilon}{n_{GB} \cdot d_{GB}} \tag{A2}$$

With the simplified formulation of the Curie-Weiss law for the dielectric constant of $SrTiO_3$ in the paraelectric phase [52]: $\varepsilon \propto \frac{1}{T}$, one gets for the ratio of Maxwell-Wagner relaxation time for material with identical processing conditions, i.e. same defect chemical scenario, but with different d, d_{gr} (thus different n_{GB}), and T (thus different σ_B), the respective subscripts 1 and 2 denoting the two different scenarios to be compared:

$$\frac{\tau_1}{\tau_2} \approx \frac{d_1}{d_2} \cdot \frac{T_2}{T_1} \cdot \frac{n_{GB,2}}{n_{GB,1}} \cdot \frac{\sigma_{B,2}}{\sigma_{B,1}} \tag{A3}$$

$\sigma_{B,1}$ emerges from the simulation results, given i for short times and the external electric field E_{ext} that is obtained by dividing U_{DC} by d:

$$\sigma_B = \frac{i}{E_{ext}} = \frac{i \cdot d}{U_{DC}} \tag{A4}$$

In general, σ_B denotes for MIEC p-type $SrTiO_3$:

$$\sigma_B = q_0 \cdot (2 \cdot \mu_{V_O^{\bullet\bullet}} \cdot [V_O^{\bullet\bullet}] + \mu_p \cdot p) \tag{A5}$$

The temperature dependence of σ_B arises from $\mu_{V_O^{\bullet\bullet}}$ according to Eq. (2), and p, whereas both $[V_O^{\bullet\bullet}]$ (that will yield the Brouwer condition arising from Eq. (1) if completely ionized acceptor is assumed) and $\mu_p \approx 0.5\ \frac{\text{cm}^2}{\text{Vs}}$ may be regarded as temperature-independent in the low-temperature regime.

With $[V_O^{\bullet\bullet}]$, $\mu_{V_O^{\bullet\bullet}}$, and μ_p known, p at T_1 can be determined from $\sigma_{B,1}$ via Eq. (A5).

According to Fermi-Dirac statstics of semiconductor physics, p denotes:

$$p(T) = N_V \cdot \exp\left(-\frac{\Delta W_p}{kT}\right) \quad \text{(A6)}$$

where N_V is the effective density of states of the valence band and ΔW_p the activation energy for the holes from the valence band.

ΔW_p can be determined from Eq. (A6), when N_V is known:

$$\Delta W_p = -kT \cdot \ln\left(\frac{p}{N_V}\right) \quad \text{(A7)}$$

Assuming temperature-independent N_V and ΔW_p, one gets for the ratio of p at two different temperatures T_1 and T_2:

$$\frac{p(T_1)}{p(T_2)} = \exp\left(-\frac{\Delta W_p}{k} \cdot \left(\frac{1}{T_1} - \frac{1}{T_2}\right)\right) \quad \text{(A8)}$$

From the thus obtained values of $\mu_{V_O^{\bullet\bullet}}$ and p at T_2, $\sigma_{B,2}$ can be calculated via Eq. (A5).

Acknowledgments

We greatly acknowledge Dr. Paul Meuffels, Dr. Herbert Schroeder, and Prof. Kurt Schroeder from Research Center Jülich for valuable discussions.

References

1. R. Waser, D. Hennings, and T. Baiatu, *Keramik*, Chapter Dielektrische Keramiken (Teubner, Stuttgart, 1994), pp. 277–388.
2. J. Claus, I. Denk, M. Leonhardt, and J. Maier, *Ber. Bunsenges. Phys. Chem.*, **101**(9), 1386 (1997).
3. F.A. Kröger and H.J. Vink, in *Solid State Physics*, Vol. 3, edited by F. Seitz and D. Turnbull (Academic Press, New York, 1956), p. 307ff.
4. G. Brouwer, *Philips Res. Rep.*, **9**, 366 (1954).
5. R. Hagenbeck, Numerical Simulation of the Defect Chemistry and Electrostatics at Grain Boundaries in Titanate Ceramics. Ph.D. Thesis, Aachen University of Technology (1998).
6. M. Fleischer, H. Meixner, and C. Tragut, *J. Am. Cer. Soc.*, **75**(6), 1666 (1992).
7. R. Waser, *J. Am. Cer. Soc.*, **74**(8), 1934 (1991).
8. R. Waser and D.M. Smyth, in *Ferroelectric Thin Films: Synthesis and Basic Properties* (Gordon and Breach, New York, 1994).
9. N.H. Chan, R.K. Sharma, and D.M. Smyth, *J. Am. Cer. Soc.*, **128**(8), 1762 (1981).
10. R. Waser and R. Hagenbeck, *Acta Mater.*, **48**, 797 (2000).
11. J. Maier, G. Schwitzgebel, and H.J. Hagemann, *J. Sol. St. Chem.*, **58**, 1 (1985).
12. H. Neumann and G. Arlt, *Ferroelectrics*, **69**, 179 (1986).
13. H.Y. Lee, S.S. Villamil, and L.C. Burton, in *Proc. 6th IEEE International Symposium of Applications of Ferroelectrics* (Lehigh University, Bethlehem, PA, 1986), pp. 361–366.
14. H.Y. Lee and L.C. Burton, *IEEE Trans. Components, Hybrids, Manuf. Technol.*, **CHMT-9**(4), 469 (1986).
15. S.S. Villamil, H.Y. Lee, and L.C. Burton, *IEEE Trans. Components, Hybrids, Manuf. Technol.*, **CHMT-12**(4), 482 (1987).
16. R. Waser, in *Proc. 1st Conference of the European Ceramic Society*, Maastricht (1989).
17. Y.-M. Chiang and T. Takagi, *J. Am. Cer. Soc.*, **73**(11), 3286 (1990).
18. H.K. Henisch, *Semiconductor Contacts* (Clarendon Press, Oxford, 1994).
19. G. Harbeke (ed.), *Polycrystalline Semiconductors*. Springer Series in Solid State Science: Vol. 57 (Springer, Berlin, 1985).
20. M. Vollmann and R. Waser, *J. Am. Cer. Soc.*, **77**(1), 235 (1994).
21. J.E. Bauerle, *J. Phys. Chem. Solids*, **30**, 2657 (1969).
22. A.K. Jonscher, *Dielectric Relaxation in Solids* (Chelsea Dielectric Press, London, 1983).
23. M. Vollmann, Elektronische Korngrenzeigenschaften Akzeptor-dotierter $SrTiO_3$-Dielektrika. Ph.D. Thesis, Aachen University of Technology (1996).
24. S. Rodewald, J. Fleig, and J. Maier, *J. Am. Cer. Soc.*, **84**(3), 521 (2001).
25. A. Tschöpe, E. Sommer, and R. Birringer, *Solid State Ionics*, **139**, 255 (2001).
26. R. Hagenbeck, L. Schneider-Störmann, M. Vollmann, and R. Waser, *Mat. Sci. Eng.*, B **39**, 179 (1996).
27. R. Hagenbeck and R. Waser, *Ber. Bunsenges. Phys. Chem.*, **101**(9), 1238 (1997).
28. M. Vollmann, R. Hagenbeck, and R. Waser, *J. Am. Cer. Soc.*, **80**(9), 2301 (1997).
29. J. Fleig and J. Maier, *J. Eur. Ceram. Soc.*, **19**, 693 (1999).
30. J. Fleig, *Solid State Ionics*, **131**, 117 (2000).
31. S.M. Sze, *Physics of Semiconductor Devices* (John Wiley & Sons, New York, 1981).
32. M. Vollmann and R. Waser, *J. Electroceramics*, **1**(1), 51 (1997).
33. R. Waser, T. Baiatu, and K.H. Härdtl, *J. Am. Cer. Soc.*, **73**(6), 1663 (1990).
34. J. Jamnik and J. Maier, *J. Electrochem. Soc.*, **145**(5), 1762 (1998).
35. J. Jamnik and J. Maier, *J. Phys. Chem. Solids*, **59**(9), 1555 (1998).
36. T. Hölbling and R. Waser, *J. Appl. Phys.*, **91**(5), 3037 (2002).
37. T. Hölbling and R. Waser (unpublished).
38. K. Szot, W. Speier, and W. Eberhardt, *Appl. Phys. Lett.*, **60**(10), 1190 (1991).
39. K. Szot and W. Speier, *Phys Rev*. B **60**(8), 5909 (1999).
40. K. Szot, W. Speier, R. Carius, U. Zastrow, and W. Beyer, *Phys Rev. Lett.*, **88**(7), 075508/1-4 (2002).
41. I. Denk, J. Claus, and J. Maier, *J. Electrochem. Soc.*, **144**, 3526 (1997).
42. C. Tragut and K.H. Härdtl, *Sens. Act.* B **4**, 425 (1991).
43. T. Bieger, J. Maier, and R. Waser, *Sens. Act.* B **7**, 763 (1992).
44. H.J. Hagemann and D. Hennings, *J. Am. Cer. Soc.*, **64**(10), 590 (1981).
45. R. Waser, T. Baiatu, and K.H. Härdtl, *J. Am. Cer. Soc.*, **73**(6), 1645 (1990).

46. R. Moos and K.H. Härdtl, *J. Am. Cer. Soc.*, **80**(10), 2549 (1997).
47. N.D. Browning, J.P. Buban, H.O. Moltaji, S.J. Pennycook, G. Duscher, K.D. Johnson, R.P. Rodrigues, and V.P. Dravid, *Appl. Phys. Lett.*, **74**(18), 2638 (1999).
48. H.P. Langtangen, *Lecture Notes in Computational Science and Engineering* (Springer, Berlin, 1999).
49. N. Söylemezoğlu, Modeling and Computation of Charge Carrier Transport and Ionization Processes in Polycrystalline $SrTiO_3$. Diploma Thesis, Aachen University of Technology (2000).
50. P. Debye and E. Hückel, *Z. Physik*, **24**, 185 (1923).
51. S. Rodewald, J. Fleig, and J. Maier, *J. Am. Cer. Soc.*, **83**(8), 1969 (2000).
52. Landolt-Börnstein, in *Zahlenwerte und Funktionen aus Naturwissenschaft und Technik*, Gruppe III: Kristall- und Festkörper, Band 16, *Ferroelektrika und verwandte Substanzen*, Teilband a: Oxide edited by K.-H. Hellwege and A.M. Hellwege (Springer, Berlin, 1981).